Journal of Ceramic Processing Research. Vol. 24, No. 5, pp. 827~834 (2023)
(Received 4 July 2023, Received in revised form 23 August 2023, Accepted 17 September 2023)
https://doi.org/10.36410/jcpr.2023.24.5.827

J O U R N A L O F
Ceramic Processing Research

Characteristics of an organic-inorganic hybrid filter consisting of $LaMn_{0.5}Fe_{0.5}O_3$ nanofibers dispersed in PAN

Hee-Seon Kim[a], Han-Jung Kim[b], Yoonkap Kim[b] and Jong-Won Yoon[a,*]
[a]*Department of Materials Science and Engineering, Dankook University, Cheonan-si 31116, Republic of Korea*
[b]*Nano Electronic Materials and Components Research Center, Gumi Electronics and Information Technology Research Institute (GERI), Gumi-si 39171, Republic of Korea*

Organic-inorganic hybrid nanofiber filters having the $LaMnO_3$ and $LaMn_{0.5}Fe_{0.5}O_3$ dispersed in polyacrylonitrile (PAN) were successfully synthesized by two-step electrospinning. In the first step, the $LaMnO_3$ and $LaMn_{0.5}Fe_{0.5}O_3$ nanofibers were synthesized by vertical-type electrospinning and heat treatment in air at 600 °C. The $LaMnO_3$ and $LaMn_{0.5}Fe_{0.5}O_3$ nanofibers have a single-phase orthorhombic crystal structure without forming secondary phases and impurities. TEM images revealed that the nanofibers were composed of nanoparticles with a diameter of about 15 nm in pure $LaMnO_3$ and 18 nm in $LaMn_{0.5}Fe_{0.5}O_3$ nanofibers. As a results of XPS analysis, $LaMn_{0.5}Fe_{0.5}O_3$ nanofibers showed more oxygen defect than $LaMnO_3$ nanofibers. In the second step, the $LaMnO_3$ and $LaMn_{0.5}Fe_{0.5}O_3$ nanofibers were homogeneously pulverized and mixed with a PAN solution to produce a filter using drum-type electrospinning. Filter performance was evaluated by the filter quality factor (QF) obtained by measuring the filtration efficiency and pressure drop of the filter. Compared to the reference (H11 nonwoven fabric), the QF increase rates of PAN, PAN/$LaMnO_3$, and PAN/$LaMn_{0.5}Fe_{0.5}O_3$ nanofiber filters were 4.1%, 12.4%, and 24.9%, respectively.

Keywords: $LaMn_{0.5}Fe_{0.5}O_3$ nanofiber, PAN, electrospinning, particulate matter filter.

Introduction

Organic-inorganic hybrid materials are functional materials with applications in optics, microelectronics, bioenergy, and environmental catalysis by combining organic and inorganic components [1]. They show excellent characteristics when used in solar cells and electrochemical devices such as electrolyte materials for secondary batteries [2-4]. Improvement in the collection of fine dust is also reported because of the synergistic effect of organic and inorganic substances in filters using metal oxide nanoparticles dispersed in organic-inorganic hybrid materials [5].

Various filters are used to remove fine dust (PM2.5), among which is the high-efficiency particulate air (HEPA) filter, a filter made of melt-blown nonwoven fabric [6]. The nonwoven material is polypropylene (PP), widely used as an air filter because of its high filtration efficiency and low-pressure drop attributed to its high porosity and dense pore size. Additionally, PP has been reported to exhibit electrostatic force around the fibers, making HEPA filters effective in the filtration of PM2.5 [7, 8]. However, the charge decays with time, causing the PM filtration performance, under certain conditions, to be remarkably reduced. Another disadvantage of HEPA filters is their relatively high air resistance [9, 10].

In order to compensate for this disadvantage, research on filters using organic nanofibers has been conducted. The materials used are mainly polymers such as polyacrylonitrile (PAN) [11], polyamide (PA) [12], nylon [13], polyurethane (PU) [14], and PVDF (polyvinylidene fluoride) [15], among which PAN has superior hydrophobicity and relative thermal stability. Polymer nanofibers are known to have high-efficiency fine dust-trapping because they have dipoles on their surfaces [16]. There are a few reports that the efficiency of collecting fine dust increases because of the release of negative ions in a filter prepared from metal oxide nanoparticles, including Al_2O_3, SiO_2, MgO, Fe_2O_3, Na_2O, TiO_2, and FeO dispersed in organic nanofibers [17-19]. Additionally, there have been reports on improving PM filtration performance through a hierarchical structure by adding magnetic Fe_3O_4 nanoparticles to organic nanofibers or coating organic nanofibers with MnO_2 [20, 21].

There is a report on improving electrical conduction by doping the A-site element of $LaFeO_3$ with Sr [22]. Also, in our previous works [23-25], primary research was reported on improving the magnetic and electrical properties of nanofibers by doping Mn or Ga in the B-site of $LaFeO_3$ nanofibers. Also, there has been a report

*Corresponding author:
Tel : +82-41-550-3536
Fax: +82-41-569-2240
E-mail: jwyoon@dankook.ac.kr

on enhancing magnetic properties in Mn-doped $BiFeO_3$ nanofibers [26]. In those papers, it was reported that as the substitution amount of the A-site or B-site increased, many oxygen vacancies occurred, which affected the magnetic/electrical properties. The $LaMnO_3$ has been developed as a sensor material with high gas sensitivity by surface adsorption to gases such as CO or NO [27, 28]. It has been reported that oxygen defects play a vital role in improving sensor performance in metal oxide gas sensors [29, 30]. Also, it has been reported that PM is formed by combining with small solid particles in the air, including organic carbon, elemental carbon, other organic matter, nitrates, sulfates, and inorganic matter [31]. Therefore, it is interesting to clarify the relationship between the adsorption of fine dust in PAN/$LaMnO_3$ and $LaMn_{0.5}Fe_{0.5}O_3$ nanofibers.

In this study, $LaMn_{0.5}Fe_{0.5}O_3$ nanofibers were fabricated by substituting up to 50% of the B site of $LaMnO_3$ nanofibers to investigate the effect of oxygen defects on filter performance. This paper aims to improve filter performance by fabricating organic-inorganic hybrid filters by dispersing $LaMnO_3$ and $LaMn_{0.5}Fe_{0.5}O_3$ nanofibers in PAN.

Experimental

Synthesis of the $LaMnO_3$ and $LaMn_{0.5}Fe_{0.5}O_3$ nanofibers

$LaMnO_3$ nanofibers were prepared using electrospinning. A sol-gel solution by dissolving polyvinylpyrrolidone (PVP, Mw = 1,300,000, Sigma Aldrich), lanthanum nitrate hexahydrate (99.999%, Sigma Aldrich), manganese nitrate tetrahydrate (≥97%, Sigma Aldrich), and *N,N*-dimethylformamide (99.8%, Sigma Aldrich) at room temperature while stirring for 2 h. To prepare $LaMn_{0.5}Fe_{0.5}O_3$ nanofibers, 50 mol% of iron nitrate nonahydrate (98%, Sigma Aldrich) was first added to a $LaMnO_3$ sol-gel solution and stirred at room temperature for 2 h.

A vertical-type electrospinning unit purchased from Nano NC Co., Ltd (Korea) was used to prepare $LaMnO_3$ and $LaMn_{0.5}Fe_{0.5}O_3$ nanofibers. The $LaMnO_3$ and $LaMn_{0.5}Fe_{0.5}O_3$ precursor solution was loaded into a 10 mL syringe with a 0.15 mm stainless-steel needle diameter. The distance between the needle tip and the collector plate was 16 cm. The collector plate was covered with aluminum foil. Electrospinning was conducted by applying a high voltage of 18.5 kV to the solution through the needle tip and fixing the flow rate to 15 μL min^{-1}. As-spun $LaMnO_3$ and $LaMn_{0.5}Fe_{0.5}O_3$ nanofibers were calcined at 600 °C in the air for 2 h with a heating rate of 5 °C min^{-1}. The heat-treated $LaMnO_3$ and $LaMn_{0.5}Fe_{0.5}O_3$ nanofibers were pulverized through a ball milling process for a uniform length.

Materials characterization

The crystal structure of the metal oxide nanofibers was characterized via X-ray diffraction measurements using an X-ray diffractometer (Ultima IV, Rigaku, Japan) with Cu Kα radiation (λ = 0.154 nm) operated at 40 kV and 30 mA. The 2θ measurement range was at 10° to 80°. To confirm the shape of the nanofibers and the fabricated filters, a field emission scanning electron microscope (SIGMA-500, Carl Zeiss, Germany) was used with an applied voltage of 20 kV. To analyze the presence and content of metal oxide nanofibers dispersed in the organic-inorganic hybrid nanofibers, energy-dispersive X-ray spectroscopy (EDS) analysis was conducted using NORAN System 7 (Thermo Fisher Scientific, USA). The morphologies of the samples were further observed by transmission electron microscopy (TEM) and high-resolution transmission electron microscopy (HRTEM) investigation by Carl Zeiss Co. (Germany) FE-TEM, Libra 200FE transmission electron microscope (TEM). X-ray photoelectron spectroscopy (XPS) was conducted using AXIS Nova (Kratos, UK) with a monochromatic Al Kα source at 1,486.6 eV, a voltage of 15 kV, and an emission current of 10 mA. The binding energy for the samples was calibrated by setting the measured binding energy of C 1*s* to 284.8 eV.

Fabrication of PAN/$LaMnO_3$ and PAN/$LaMn_{0.5}Fe_{0.5}O_3$ nanofibers filter

PAN solution was prepared using polyacrylonitrile (PAN, M_W = 150,000) and *N,N*-dimethylformamide (99.8%, Sigma Aldrich) by stirring at 60 °C for 24 h. Then the pulverized $LaMnO_3$ and $LaMn_{0.5}Fe_{0.5}O_3$ nanofibers of 0.2 g were added into the PAN solution with stirring at room temperature for 2 h. In this case, an ESR100D drum-type equipment (Nano NC Co., Ltd., Korea) was used for electrospinning. The distance between the needle tip and the collector was 20 cm. A high voltage of 15 kV was applied through the needle tip, the flow rate was fixed at 1 mL/h, and the rotation speed of the collector was at 500 rpm. A commercial polypropylene (PP) material (H11 nonwoven fabric) was used to cover the collector and act as a substrate for the filter.

Figure 1(a) shows a schematic diagram of the filter fabrication process using the PAN/$LaMnO_3$ and PAN/$LaMn_{0.5}Fe_{0.5}O_3$ nanofibers. Also, Fig. 2(b) is a drawn picture of PAN/$LaMnO_3$ and PAN/$LaMn_{0.5}Fe_{0.5}O_3$ nanofibers filter dispersed on an H11 nonwoven fabric.

For the fabrication of nanofiber filters with optimized density, the accumulation time was adjusted to 0, 1, 3, 5, 10, and 20 min, as shown in Fig. 1(c). As the accumulation time increased, the filter color changed to dark gray.

Particulate matter filtration test

The fine dust filtration performance of the PAN/$LaMnO_3$ and PAN/$LaMn_{0.5}Fe_{0.5}O_3$ nanofibers filter with reference to the device proposed in the reported

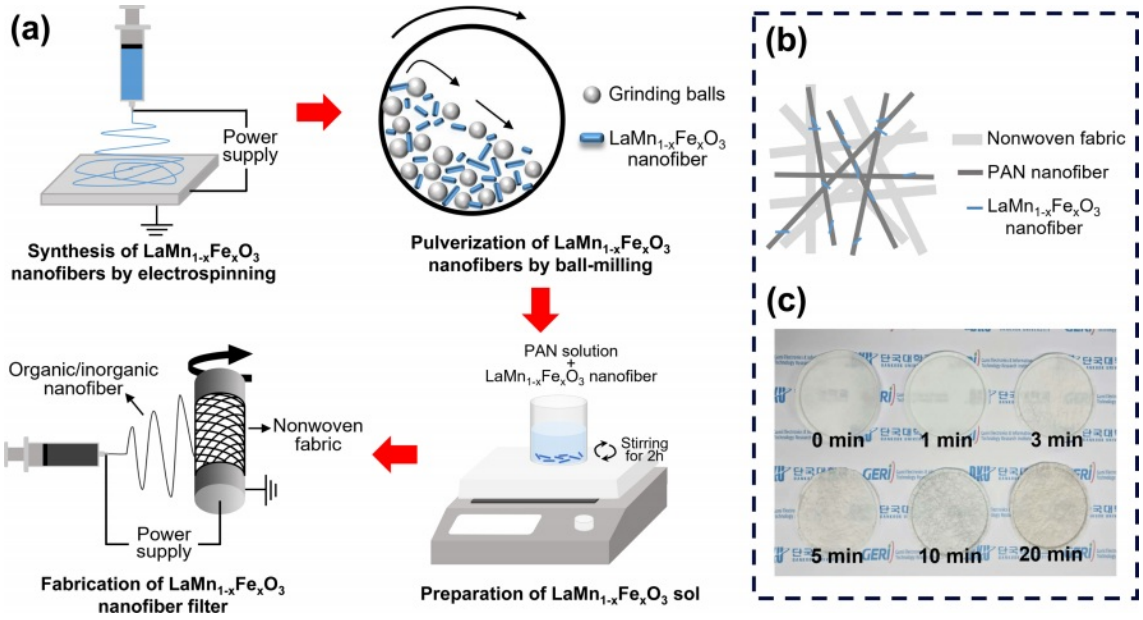

Fig. 1. (a) Schematic of the manufacturing process of the $LaMnO_3$ and $LaMn_{0.5}Fe_{0.5}O_3$ nanofibers filter, (b) Schematic of the PAN/$LaMnO_3$ and PAN/$LaMn_{0.5}Fe_{0.5}O_3$ nanofibers filter dispersed on an H11 nonwoven fabric, (c) Actually pictures of the PAN/$LaMnO_3$ and PAN/$LaMn_{0.5}Fe_{0.5}O_3$ nanofibers filter according to accumulation time.

works of literature was evaluated as shown in Fig. SI 1 [32]. A light-scattering-type PM sensor (PM2007, Wuhan Cubic Optoelectronic Co. Ltd.) was used calibrated using standard test equipment before the test. Incense smoke was used as fine dust, composed of particles with a diameter of 0.3 to 10.0 μm as confirmed by optical measurements (Optical Particle Sizer 3330, TSI) [32]. Pressure at a flow rate of 22 L min^{-1} was supplied to the filters through a vacuum pump (Rocker300), and the pressure drops across the filters were measured using a differential pressure meter (Testo 510, Testo Inc.). PM filtration efficiency can be calculated by measuring the concentration of incense smoke before and after the filters as summarized in the following formula: efficiency, % = ((C1 − C2)/C1) × 100 [33]. All samples for testing were prepared in a circular shape with a diameter of 60 mm. A simple air purifier using a handmade plastic jig was set up, and a DC fan was used to test the air purification performance (speed) in the chamber. The fabricated air purifier and wireless PM sensor were placed in a polycarbonate chamber with a volume of ~400 L, and a certain amount of smoke was supplied. The air purifier was operating at a constant driving voltage, and the change in the concentration of fine dust in the chamber was monitored in real-time. The initial concentration of fine dust supplied into the chamber was ~250 μg m^{-3}.

Results and Discussion

Figure 2a shows the XRD patterns of a PAN and the $LaMnO_3$ and $LaMn_{0.5}Fe_{0.5}O_3$ nanofibers. The $LaMnO_3$ and $LaMn_{0.5}Fe_{0.5}O_3$ nanofibers have a single-phase

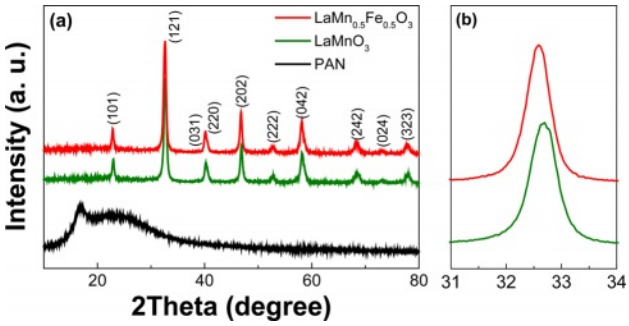

Fig. 2. (a) XRD patterns of the PAN, $LaMnO_3$, and $LaMn_{0.5}Fe_{0.5}O_3$ nanofibers; (b) Enlarged XRD patterns.

orthorhombic crystal structure without forming secondary phases and impurities. Since PAN is an organic material, the crystal peak is not expressed, and its peak appears in a typical broad form similar to that of the previously reported XRD peak of PAN. The (121) peaks near 32.6° shift to a lower angle compared to $LaMnO_3$ (as seen in Fig. 2b). The peak shift is due to substituting with Fe^{3+} (0.645 Å), which has a larger ionic radius than that of Mn^{3+} (0.58 Å). The average crystallite size of the Fe-substituted $LaMnO_3$ nanofibers was calculated using Scherrer's formula, and the average crystal size of the $LaMnO_3$ and $LaMn_{0.5}Fe_{0.5}O_3$ nanofibers is 15.25 and 18.43 nm, respectively.

Figure 3(A) and (B) display typical TEM images of the $LaMnO_3$ and $LaMn_{0.5}Fe_{0.5}O_3$ nanofibers. It is evident from a close examination of TEM images of the $LaMnO_3$ (Fig. 3(A)) and $LaMn_{0.5}Fe_{0.5}O_3$ nanofibers (Fig. 3(B)) that a single nanofiber was composed of several nanoparticles. Further, it can be observed in

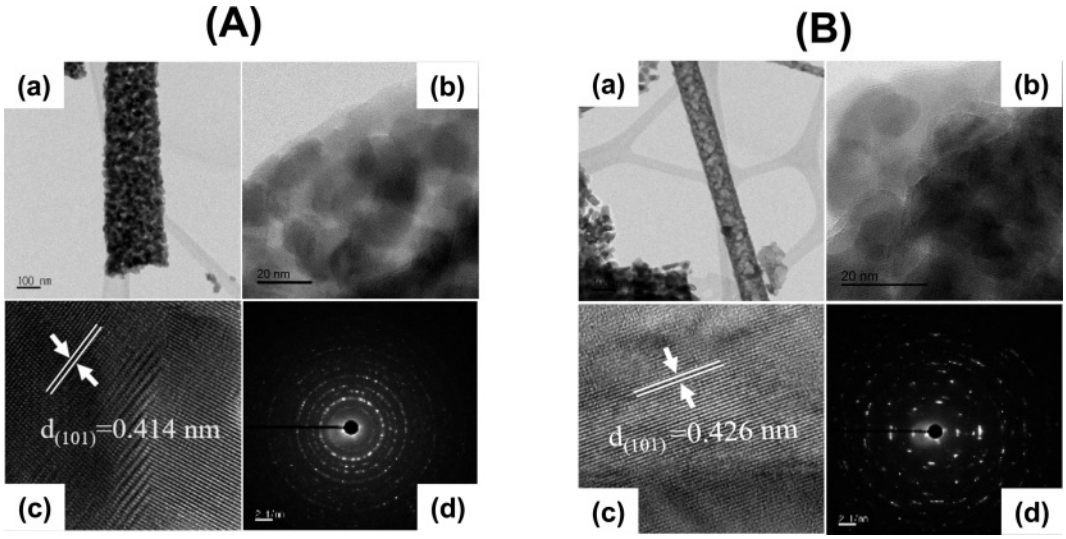

Fig. 3. TEM images at low and high magnification: (A) $LaMnO_3$ nanofibers; (B) $LaMn_{0.5}Fe_{0.5}O_3$ nanofibers.

Fig. 3A(b) and 3B(b) that the nanofibers are made up of homogeneously distributed nanoparticles of an average diameter of about 15 nm (Fig. 3A(b)) and 18 nm (Fig. 3B(b)), respectively. It can be noticed that the crystallite sizes calculated via Scherrer's formula from XRD measurements are in good agreement with nanoparticulate sizes observed by TEM. As shown in Fig. 3A(c) and Fig. 3B(c), the interplanar distance of the (101) plane was 0.414 nm for pure $LaMnO_3$ and 0.426 nm for $LaMn_{0.5}Fe_{0.5}$, respectively. The increase of interplanar spacings with Fe substituting is due to the difference in ionic radius between Mn^{3+} (0.58 Å) and Fe^{3+} ions (0.645 Å).

Figure 4(a) and (c) show FESEM images of the $LaMnO_3$ and $LaMn_{0.5}Fe_{0.5}O_3$ nanofibers. It was confirmed that their diameters are in the range of 100-150 nm. Additionally, the FESEM images of the $LaMnO_3$ and $LaMn_{0.5}Fe_{0.5}O_3$ nanofibers measured after the ball milling process are shown in Fig. 4(b) and (d). The length of the $LaMnO_3$ and $LaMn_{0.5}Fe_{0.5}O_3$ nanofibers was 0.5 to 1.5 μm. The ball milling process was conducted to homogeneously disperse the inorganic $LaMnO_3$ and $LaMn_{0.5}Fe_{0.5}O_3$ nanofibers in organic PAN.

XPS analysis was conducted to confirm the surface composition and oxidation state of the metal ions in the $LaMnO_3$ and $LaMn_{0.5}Fe_{0.5}O_3$ nanofibers. Figure 5 shows the XPS analysis results of La 3*d*, Mn 2*p*, Fe 2*p*, and O 1*s* in the $LaMnO_3$ and $LaMn_{0.5}Fe_{0.5}O_3$ nanofibers. As shown in the XPS spectrum of La 3*d* (Fig. 5(a)), the La $3d_{5/2}$ and La $3d_{3/2}$ peaks have binding energies of 834.03 and 850.9 eV, respectively, and the binding energy difference between the peaks is 16.06 eV, which was confirmed to represent a typical +3 valence state of La [34-36]. Figure 5(b) exhibits the XPS analysis result of Fe 2*p* in the $LaMn_{0.5}Fe_{0.5}O_3$ nanofibers substituted with 50 mole% Fe. The Fe $2p_{3/2}$ and Fe $2p_{1/2}$ peaks have a binding energy of 710.7 and 724.6 eV,

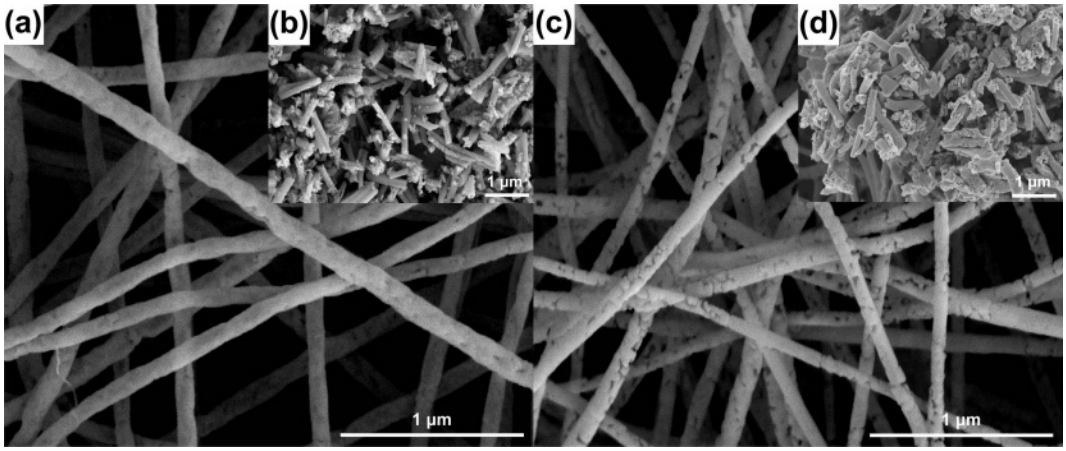

Fig. 4. SEM images: $LaMnO_3$ nanofiber (a) before ball-milling and (b) after ball-milling; $LaMn_{0.5}Fe_{0.5}O_3$ nanofiber (c) before ball-milling and (d) after ball-milling.

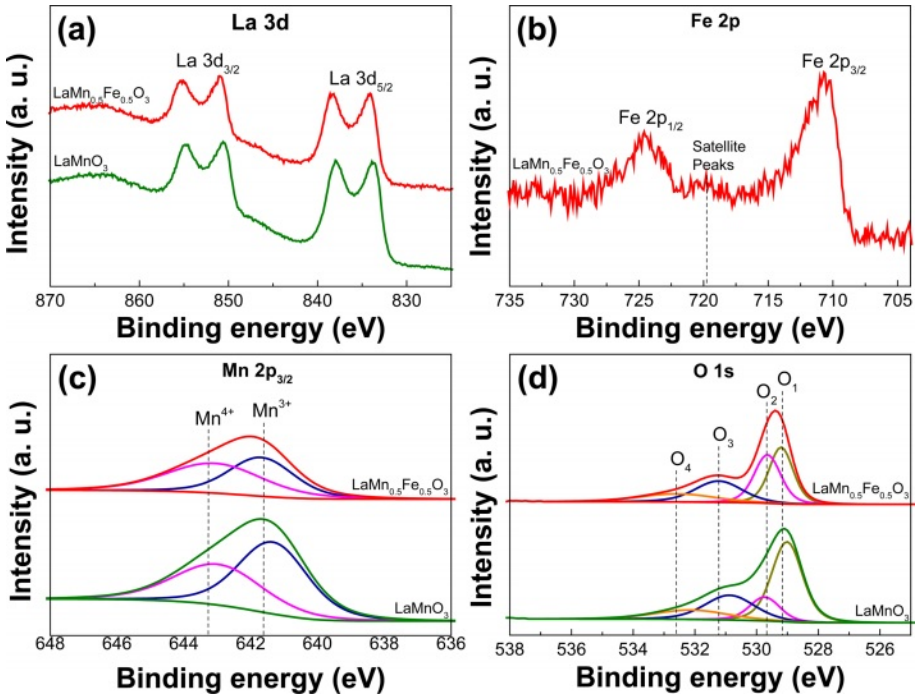

Fig. 5. XPS spectra of the PAN/$LaMnO_3$ and PAN/$LaMn_{0.5}Fe_{0.5}O_3$ nanofibers (a) La 3d and (b) Fe 2p; curve fitting of (c) Mn $2p_{3/2}$ and (d) O 1s.

respectively, and the binding energy difference between the peaks is 13.9 eV. Additionally, it observed that a satellite peak at 719.5 eV exists between the Fe $2p_{3/2}$ and Fe $2p_{1/2}$ peaks [37]. This satellite peak indicates that valence number of Fe is +3. Figure 5(c) shows the Gaussian-Lorentzian curve fitting result of the Mn $2p_{3/2}$ peak. Compared with the Mn $2p_{3/2}$ peak in the $LaMnO_3$ nanofibers, the intensity of the Mn $2p_{3/2}$ peak in the $LaMn_{0.5}Fe_{0.5}O_3$ nanofibers was lower, which is a result of the 50 mol% Fe^{3+} ions being substituted for the Mn^{3+} ions. The +3 and +4 valence peaks of Mn appear at 641.3-641.6 eV and 643.0-643.4 eV, respectively. The area ratio of Mn^{4+}/Mn^{3+} in the curve-fitting result of the Mn$2p_{3/2}$ peak of the $LaMnO_3$ and $LaMn_{0.5}Fe_{0.5}O_3$ nanofibers is 0.72 and 1.14, respectively, indicating that the amount of Mn^{4+} increased in the samples substituted with 50 mol% Fe. Figure 5d shows the curve-fitting result of the O 1*s* peak. Four peaks appear at a wide binding energy range of 529.2-532.6 eV, indicating various chemical bonding states of O 1*s*. The O_1 peak

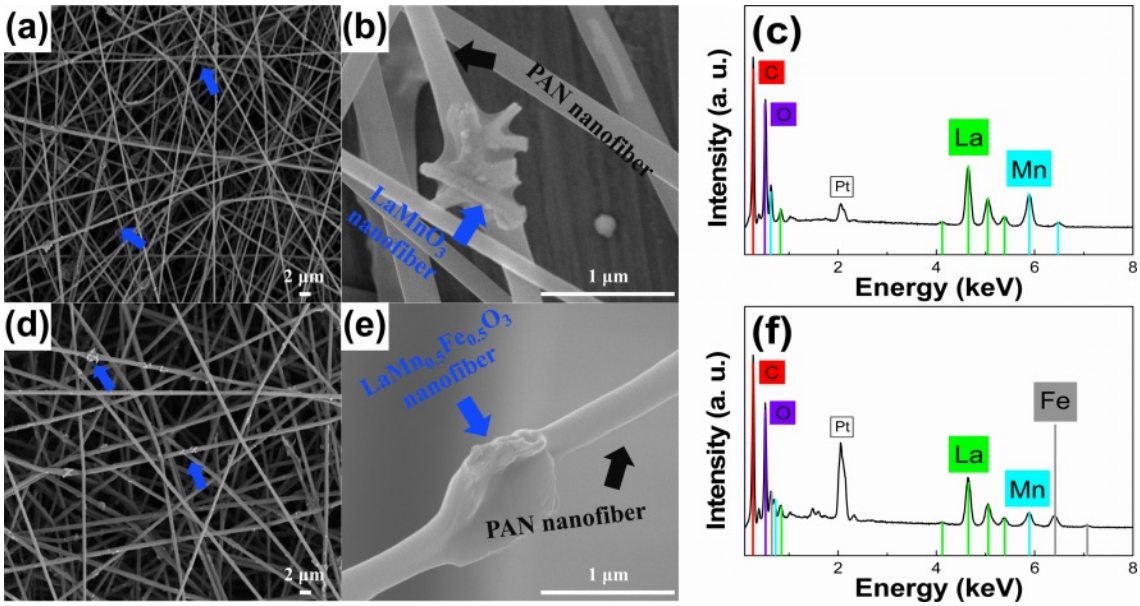

Fig. 6. (a)-(b) SEM images of PAN/$LaMnO_3$ and (c) its EDS spectrum; (d)-(e) SEM images of $LaMn_{0.5}Fe_{0.5}O_3$ nanofibers nanofiber and (f) its EDS spectrum.

is attributed to oxygen in the crystal lattice [38], such as that of La-O and Fe-O in the $LaMnO_3$ and $LaMn_{0.5}Fe_{0.5}O_3$ nanofibers. The O_2 peaks correspond to oxygen defects, the O_3 peak is related to the hydroxyl group, and the O_4 peak is associated with the nitrate group [39, 40]. The area of the O_2 peak in the $LaMn_{0.5}Fe_{0.5}O_3$ nanofibers is larger than that of the O_2 peak in the $LaMnO_3$ nanofibers. This result indicates that Fe^{3+} substitution into $LaMnO_3$ induces increasing of the amount of Mn^{4+} and causes the increase in the amount of adsorbed oxygen for having electronic compensation. These results agree well with the previously reported results of $LaFeO_3$ doped with 15% Mn [24].

Figure 6(a)-(c) display SEM images and EDS spectra of the PAN/$LaMnO_3$ nanofiber. The diameter of PAN is 300-400 nm, and the length of the $LaMnO_3$ nanofibers is 0.5-1.0 μm. Additionally, La, Mn, and O were detected on the basis of EDS analysis results, as shown in Fig. 6(c). Figure 6(d)-(f) represent the SEM images and EDS spectra of the PAN/$LaMn_{0.5}Fe_{0.5}O_3$ nanofibers. Moreover, La, Mn, Fe, and O were detected, and Mn and Fe were present in a ratio of 5:5 based on EDS analysis results. Pt was also seen from the coating materials for SEM measurements.

Filter performance was evaluated by measuring the filtration efficiency and pressure drop across the filters using handmade equipment. Furthermore, the filter quality factor (QF) was calculated using the following equation $QF = -\ln[1 - E\ (\%)]/\Delta P$. Where E is filter efficiency, and ΔP is pressure drop. For higher QF values, finding out the optimal density of the PAN/$LaMnO_3$ and PAN/$LaMn_{0.5}Fe_{0.5}O_3$ nanofiber filter is essential. In this report, experiments were conducted to obtain optimized density values according to changes in accumulation time. The time was set at 0, 1, 3, 5, 10, and 20 min to determine the effect of the accumulation time on the filter performance. As shown in Fig. 7(a) and (b), when the accumulation time is 3 min, the PAN/$LaMnO_3$ nanofibers filter showed the highest performance with filtration efficiency, pressure drop, and QF of 86.65%, 62 Pa, and 0.03248 Pa^{-1}, respectively. Also, the PAN/$LaMn_{0.5}Fe_{0.5}O_3$ nanofibers filter represented the highest QF when the accumulation time was 3 min, as shown in Fig. 7(c) and (d). Thus, the optimal accumulation time for filter performance was 3 min both the PAN/$LaMnO_3$ and PAN/$LaMn_{0.5}Fe_{0.5}O_3$ nanofiber filters.

Figure 8(a) compares the filtration efficiency and pressure drop results of the reference, PAN, PAN/$LaMnO_3$, and PAN/$LaMn_{0.5}Fe_{0.5}O_3$ filters. Figure 8(b) displays the QF derived from the formula $QF = -\ln[1 - E\ (\%)]/\Delta P$. The PAN/$LaMnO_3$ and PAN/$LaMn_{0.5}Fe_{0.5}O_3$ nanofiber filters showed a higher QF than the reference (H11 nonwoven fabric) and PAN-only filters. Compared to H11 nonwoven fabric, the QF increase rates of PAN, PAN/$LaMnO_3$, and PAN/$LaMn_{0.5}Fe_{0.5}O_3$ nanofiber filters were 4.1%, 12.4%, and 24.9%, respectively. The increased QF in PAN/$LaMnO_3$, and PAN/$LaMn_{0.5}Fe_{0.5}O_3$ nanofiber is estimated to be due to the adsorption of fine dust on the inorganic surface ($LaMnO_3$ or $LaMn_{0.5}Fe_{0.5}O_3$) with oxygen

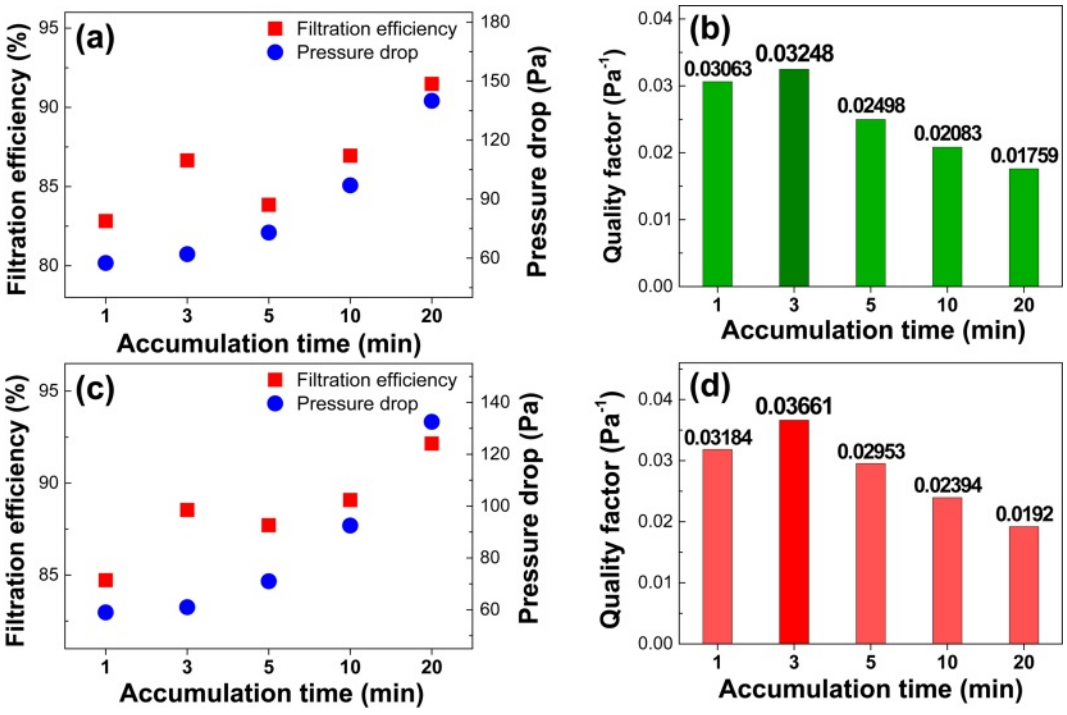

Fig. 7. Filtration performance test by accumulation time: PAN/$LaMnO_3$ nanofiber filter (a) Efficiency and Pressure drop (b) Quality factor; PAN/$LaMn_{0.5}Fe_{0.5}O_3$ nanofibers filter (c) Efficiency and Pressure drop (d) Quality factor results.

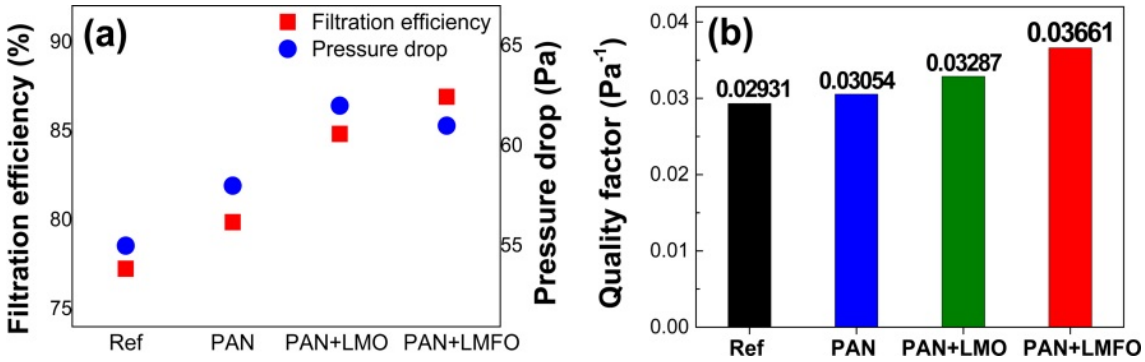

Fig. 8. (a) Efficiency and Pressure drop and (b) Quality factor results of reference (H11 nonwoven fabric), PAN, PAN/$LaMnO_3$, and PAN/$LaMn_{0.5}Fe_{0.5}O_3$ nanofibers filter.

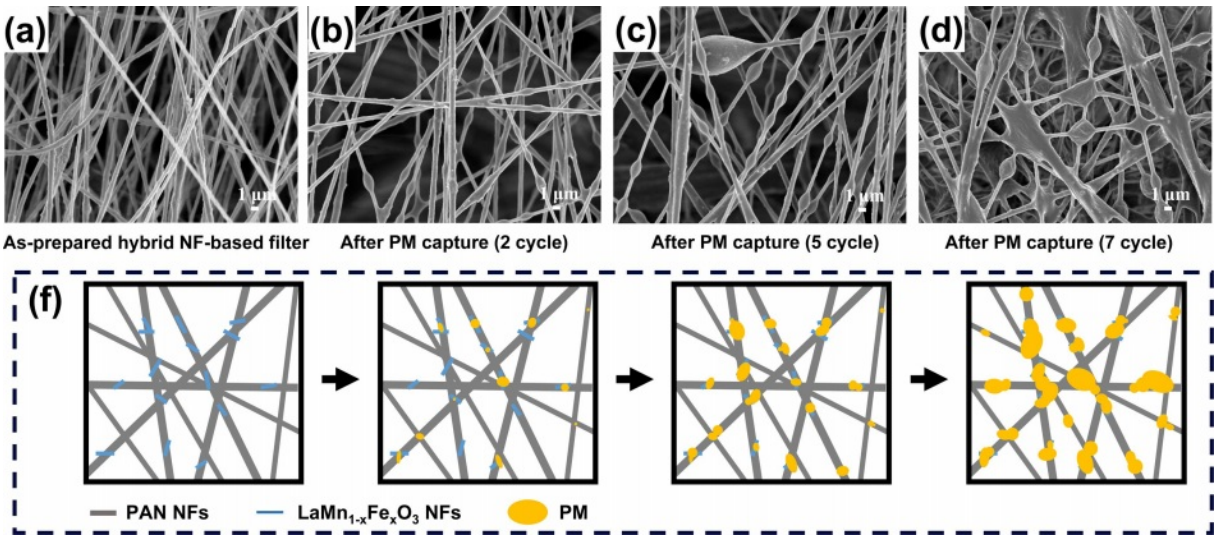

Fig. 9. (a)-(d) FE-SEM image of PAN/$LaMn_{0.5}Fe_{0.5}O_3$ filter with increasing PM capturing cycle, (f) Schematic of the captured PM surface on PAN/$LaMn_{0.5}Fe_{0.5}O_3$ nanofibers filter at different cycles.

vacancies and the change of the electrostatic force on the surface of organic PAN. However, the detailed mechanism needs further in-depth. As mentioned in the XPS section, Fe substitution in $LaMnO_3$ increased in the amount of oxygen vacancy. Therefore, the dispersion of $LaMn_{0.5}Fe_{0.5}O_3$ nanofibers in PAN was very useful for improving filter performance. Figure 9(a)-(d) shows the SEM images of the PAN/$LaMn_{0.5}Fe_{0.5}O_3$ nanofiber filters versus cycle time during fine dust filtration. Over time, the fine dust filtered by the PAN/$LaMn_{0.5}Fe_{0.5}O_3$ nanofiber filters forms a large mass of particulate matter (PM). Also, Figure 9(f) displays the schematic of the captured PM on PAN/$LaMn_{0.5}Fe_{0.5}O_3$ nanofibers filter at different cycles.

Conclusions

In this study, an organic-inorganic hybrid filter of PAN/$LaMnO_3$ and PAN/$LaMn_{0.5}Fe_{0.5}O_3$ nanofiber was successfully synthesized by a two-step electrospinning method. The $LaMnO_3$ and $LaMn_{0.5}Fe_{0.5}O_3$ nanofibers have a single-phase orthorhombic crystal structure without forming secondary phases and impurities. The diameter of $LaMnO_3$ and $LaMn_{0.5}Fe_{0.5}O_3$ nanofibers ranged from 100 to 150 nm. Also, the $LaMnO_3$ and $LaMn_{0.5}Fe_{0.5}O_3$ nanofiber was found to have a one-dimensional structure in which nanoparticles of 15 nm and 18 nm were aggregated. According to the XPS analysis, in the case of $LaMn_{0.5}Fe_{0.5}O_3$ nanofibers, the amount of oxygen defects increased due to Fe substitution of $LaMnO_3$. As a result of the filter performance test, both PAN/$LaMnO_3$ and PAN/$LaMn_{0.5}Fe_{0.5}O_3$ showed the highest QF at 3 min. of electrospinning accumulation time. The PAN/$LaMnO_3$ and PAN/$LaMn_{0.5}Fe_{0.5}O_3$ nanofiber filters showed a higher QF than the reference (H11 nonwoven fabric) and PAN-only filters. Compared to the reference, QF increase rates of PAN, PAN/$LaMnO_3$, and PAN/$LaMn_{0.5}Fe_{0.5}O_3$ nanofiber filters were 4.1%, 12.4%, and 24.9%, respectively. The difference between the QF value of the $LaMnO_3$ and $LaMn_{0.5}Fe_{0.5}O_3$ nanofibers is estimated to be due to the rise in the release of negative ions. Therefore, the dispersion of $LaMn_{0.5}Fe_{0.5}O_3$ nanofibers in PAN was very useful for improving filter

performance.

Acknowledgement

This research was supported by Basic Science Research Program through the National Research Foundation of Korea (NRF) funded by the Ministry of Education (2018R1D1A3B07050056). This work was partially supported by the Technology Innovation Program (Advanced Technology Center Plus, 20018017) funded by the Ministry of Trade, Industry & Energy (MOTIE, Korea).

References

1. S.H. Mir, L.A. Nagahara, T. Thundat, P.M. Tabari, H. Furukawa, and A. Khosla, J. Electrochem. Soc. 165 (2018) B3137-B3156.
2. L. Zhang, Y. Gong, Q. Hu, L. Wang, J. Wu, and L. Yu, J. Phys. Chem. C 125 (2021) 1441-1446.
3. S. Singh, H. Chen, S. Shahrokhi, L.P. Wang, C.-H. Lin, X. Guan, A. Tricoli, Z.J. Xu, and T. Wu, ACS Energy Lett. 5 (2020) 1487-1497.
4. H. Zhao, N. Deng, W. Kang, and B. Cheng, Chem. Eng. J. 390 (2020) 124571.
5. X. Zhao, Y. Li, T. Hua, P. Jiang, X. Yin, J. Yu, and B. Ding, ACS Appl. Mater. Interfaces 9 (2017) 12054-12063.
6. T.-T. Li, W. Fan, X. Cen, Y. Wang, B.-C. Shiu, H.-T. Ren, H.-K. Peng, Q. Jiang, C.-W. Lou, and J.-H. Lin, Nanomaterials 10 (2020) 2025.
7. H. Zhang, J. Liu, X. Zhang, C. Huang, and X. Jin, RSC Adv. 8 (2018) 7932-7941.
8. M.A. Hassan, B.Y. Yeom, A. Wilkie, B. Pourdeyhimi, and S.A. Khan, J. Membr. Sci. 427 (2013) 336-344.
9. R. Thakur, D. Das, and A. Das, Fibers Polym. 15 (2014) 1436-1443.
10. W. Jasper, J. Hinestroza, A. Mohan, J. Kim, B. Shiels, M. Gunay, D. Thompson, and R. Barker, J. Aerosol Sci. 37 (2006) 903-911.
11. H. Gao, Y. Yang, O. Akampumuza, J. Hou, H. Zhang, and X. Qin, Environ. Sci.: Nano 4 (2017) 864-875.
12. N. Wang, X. Wang, B. Ding, J. Yu, and G. Sun, J. Mater. Chem. 22 (2012) 1445-1452.
13. J. Xu, C. Liu, P.-C. Hsu, K. Liu, R. Zhang, Y. Liu, and Y. Cui, Nano Lett. 16 (2016) 1270-1275.
14. W. Sambaer, M. Zatloukal, and D. Kimmer, Chem. Eng. Sci. 82 (2012) 299-311.
15. J. Lee, and J. Kim, Polymer 12 (2020) 721.
16. H.-J. Kim, S.J. Park, C.S. Park, T.-H. Le, S.H. Lee, T.H. Ha, H.-I Kim, J. Kim, C.-S. Lee, H. Yoon, and O.S. Kwon, Chem. Eng. J. 339 (2018) 204-213.
17. X.L. Zhao, Y. Li, T. Hua, P. Jiang, X. Yin, J. Yu, and B. Ding, Acs Appl. Mater. Interfaces 9 (2017) 12054-12063.
18. X. Zhu, Z. Dai, K. Xu, Y. Zhao, and Q. Ke, Macromol. Mater. Eng. 304 (2019) 1900350.
19. D. Cho, A. Naydich, M.W. Frey, and Y.L. Joo, Polymer 54 (2013) 2364-2372.
20. J. Kim, S.C. Hong, G.N. Bae, and J.H. Jung, Environ. Sci. Technol. 51 (2017) 11967-11975.
21. M. Hu, L. Yin, H. Zhou, L. Wu, K. Yuan, B. Pan, Z. Zhong, and W. Xing, J. Mem. Sci. 605 (2020) 118094.
22. A.S. Nesaraj, S. Dheenadayalan, I.A. Raj, and R. Pattabiraman, J. Ceram. Process. Res. 13 (2012) 601-606.
23. W.Y. Lee, H.J. Yun, and J.-W. Yoon, J. Alloy. Compd. 583 (2014) 320-324.
24. J.-H. Jeong, C.-G. Song, K.-H. Kim, W. Sigmund, and J.-W. Yoon, J. Alloy. Compd. 749 (2018) 599-604.
25. T. Moon, W.-Y. Lee, C.-J. Choi, and J.-W. Yoon, Appl. Phys. Lett. 105 (2014) 153103.
26. G.M. Bak, C.-G. Song, and J.-W. Yoon, J. Ceram. Process. Res. 19 (2018) 253-256.
27. R. Sorita and T. Kawano, Sens. Actuator B 40 (1997) 29-32.
28. M. Shen, Z. Zhao, J. Chen, Y. Su, J. Wang, and X. Wang, J. Rare Earths 31 (2013) 119-123.
29. M. Al-Hasem, S. Akbar, and P. Morris, Sens. Actuator B 301 (2019) 126845.
30. J.W. Yoon, M.L. Grilli, E.D. Bartolomeo, R. Ploini, and E. Traversa, Sens. Actuator B 76 (2001) 483-488.
31. Z. Yang, Y. Zhen, Y. Feng, X. Jiang, Z. Qin, W. Yang, and Y. Qie, J. Colloid. Interface. Sci. 635 (2023) 598-610.
32. C. Liu, P.-C. Hsu, H.-W. Lee, M. Ye, G. Zheng, N. Liu, W. Li, and Y. Cui, Nat. Commun. 6 (2015) 6205.
33. C.-H. Hung, and W.W.-F. Leung, Sep. Purif. Technol. 79 (2011) 34-42.
34. E. Cao, Y. Yang, T. Cui, Y. Zhang, W. Hao, L. Sun, H. Peng, and X. Deng, Appl. Surf. Sci. 393 (2017) 134-143.
35. R.D. Kumar, R. Thangappan, and R. Jayavel, J. Phys. Chem. Solid. 101 (2017) 25-33.
36. K.M. Parida, K.H. Reddy, S. Martha, D.P. Das, and N. Biswal, Int. J. Hydrogen Energy 35 (2010) 12161-12168.
37. G. Dong, G. Tan, W. Liu, A. Xia, and H. Ren, J. Mater. Sci. Technol. 30 (2014) 365-370.
38. J.W. Yoon, E.D. Bartolomeo, and E. Traversa, J. Electroceram. 26 (2011) 28-31.
39. H. Su, L. Jing, K. Shi, C. Yao, and H. Fu, J. Nanopart. Res. 12 (2010) 967-974.
40. J.F. Moulder, W.F. Stikle, P.E. Sobol, K.D. Bomben, and J. Chastain, Handbook of X-ray Photoelectron Spectroscopy, Eden Prairie, MN, 1992.